Field ionization intensity used to measure local pressure in gas flows

Felix Sharipov, Irina Martin Graur, Evelyne Salançon

Field ionization intensity used to measure local pressure in gas flows

Felix Sharipov[a], Irina Graur[b], Evelyne Salançon[c]

[a]Departamento de Fisica, Universidade Federal do Parana, 81531-980 Curitiba, Brazil
[b]IUSTI Aix-Marseille Univ CNRS UMR7343 France
[c]CINaM Aix-Marseille Univ CNRS UMR7325 France

Abstract

A coaxial ion source produces an ion beam via field effect in a gas flow through a coaxial microchannel structure. Measuring the intensity of ion emission under an electric voltage condition reveals the pressure at the tip of the coaxial structure, where ionization occurs. The spatial resolution of the measurements is defined by the volume into which the position of the tip fits, here estimated as a cube with an edge of 10 μm. The pressure at the tip is also obtained analytically as a function of the throughput through the coaxial structure. The theoretical and experimental pressure values reported in the present work are in agreement between them within the geometric uncertainties of the coaxial structure itself.

Keywords: Coaxial Ion Source, Flow rate, Local pressure gauge, Field ionization, Gas expansion, Channel Gas flow

1. Introduction

Local gas density or pressure in either free gas expansion or gas jets is often measured via optical diffusion [1] or laser-induced fluorescence, by adding acetone to the gas (see for example Refs. [2, 3]). It would greatly enrich the optical measurement of gas parameters if direct experimental determination of local gas pressure could be achieved. The question is: what kind of local pressure gauge could be used, and with what spatial resolution? Our hypothesis here is that, given the relationship between intensity of field ionization and local gas pressure, field ionization measurements can reliably be used as a local pressure reading.

Field ionization is well-known as a way to explore crystallographic surfaces of a metal tip in a field ion microscope [4–7], or to produce ion beams for instrumentation termed Gas Field Ion Sources, such as Coaxial Ion Sources (CIS) (see e.g. Refs.[8–10]). With these latter, the gas is locally injected into the ion production zone through the coaxial micro-channel structure. Ref. [8] showed that this structure permits high current intensities to be obtained when the pressure is maintained low enough for unimpeded beam propagation. In addition,

Email addresses: sharipov@fisica.ufpr.br (Felix Sharipov[a]), irina.martin@univ-amu.fr (Irina Graur[b]), evelyne.salancon@univ-amu.fr (Evelyne Salançon[c])

it was shown that gas flow regimes do not modify field ion efficiency. In the CIS described in Ref. [8], the ion current intensity measured under "static" pressure without gas injection was 300 times lower than the intensity measured under dynamic pressure, with the gas injected through the coaxial structure. What we seek to determine here is whether the ion current intensity measured in a setup involving a coaxial ion source corresponds to the local pressure reading at the tip. However, we do not seek to determine the gas supply by measuring the intensity on a one-to-one basis, but only the local pressure with a relative reading, by comparing the intensity under "static" pressure and the intensity under flow. The question is whether, in the flow, some mechanisms such as recombination, speed of molecules or other factors could influence the measurement of intensity.

The present paper is organized as follows. First, experimental details are given in Section 2, with a description of the setup including the CIS and the methods used to measure throughput and ionization intensity. The modeling of gas flow is then explained in Section 3, showing how the pressure can be expressed anywhere in the chamber given the initial conditions. The results obtained for the different structures and methods are presented in Section 4. This leads to an in-depth discussion in Section 5 on measurement uncertainties and on estimation of the spatial resolution of the pressure gauge.

2. Experimental details

2.1. Setup

The coaxial ion source [8, 11–14] mounted at the Marseille Interdisciplinary Nanoscience Center (CINaM) of Aix-Marseille University is a deliberate leak between a high-pressure (inlet) vacuum chamber (p_{in}) with a volume of $V_{in} = (0.30 \pm 0.05)$ L and a low-pressure (outlet) vacuum chamber (p_{out}) with a volume of $V_{out} = (67 \pm 5)$ L. A metal tip is placed at the outlet of this leak on the low-pressure chamber side. In the present work, the same experimental setup as that presented in Ref.[8] is used. A scheme of the setup is shown in Figure 1, where $L = 6$ mm is the length of the stainless-steel tube. Two tubes with different internal diameters were used: $d_2 = (150+30)\,\mu$m and $(170 + 30)\,\mu$m. Note that the uncertainty of d_2 is only positive, the smallest value is guaranteed by the manufacturer.

A tungsten wire with a diameter of $d_1 = (125 \pm 13)\,\mu$m was inserted into the tube with an internal diameter of d_2. The tungsten wire ends in a tip which emerges at position $H = (130 \pm 10)\,\mu$m from the end of the tube. This position is set under an optical microscope and the wire is glued at this position. The glue does not affect the flow because it is offset from the flow, see Ref.[8] for more explanation. The tungsten tip is covered at its top with a thin layer of palladium, which protects the tungsten from corrosion and allows it to work longer. Finally the tips have a spherical shape with a radius of around (100 ± 20) nm. The tips are observed by scanning electron microscope (SEM) before and after experiments. I(V) curves

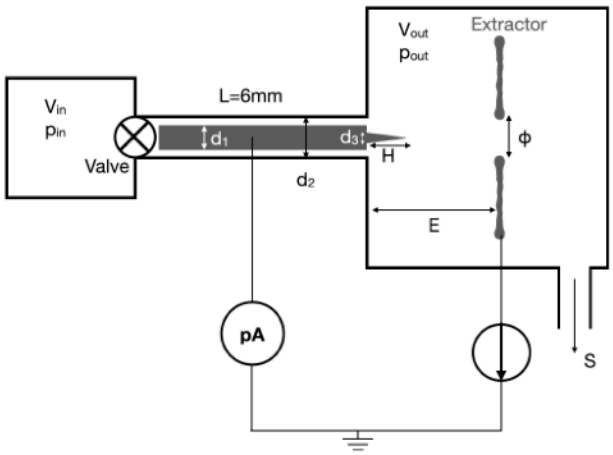

Figure 1: Scheme of the experimental setup: the Coaxial Ion Source (CIS) is placed between the inlet pressure chamber and the outlet pressure chamber, where ionization takes place.

are systematically made to check that the shape of the tip has not evolved between experiments. To simplify modeling, the shape of the tip is assumed to be a cone with a base diameter of $d_3 = d_1/2$ and a height of H.

Table 1 describes the different structures involved in the study. The uncertainty calculated in Section 5 takes into account the dispersion of the geometrical structures. For example, when the wire is inserted into the capillary, it may neither be perfectly centered nor straight throughout the capillary, i.e. the centering of the tip and its positioning in the plane are accurate to within 10 μm.

After baking, both chambers can be evacuated down to ultrahigh vacuum conditions by a turbomolecular pump (TwisTorr305, Agilent).

To measure inlet pressure, a membrane-based gauge (ED 510/421.411/025 from Haenni) is used. Outlet pressure is measured by a full-range gauge (Varian). The electric field is imposed by electrically grounding the CIS through a pico-ammeter (Keithley, Model 427) and an extractor is electrically polarized to a negative voltage (reversible, low-ripple module MPS30 from Spellman). The extractor represented by the plane in front of the tip in Figure 1 is a metal disc 3.5 cm in diameter with a hole $\phi = 1$ mm in diameter placed at a distance $E = 1$ mm from the tip.

2.2. *Throughput measurement*

The throughput q [15] of the tube determines the flow-field in the outlet chamber so that the throughput knowledge gives us the pressure at the tip. However, the tungsten wire inside the tube is not straight, hence the gap shape between them is unknown. This makes it impossible to calculate the throughput numerically. Here, the throughput is obtained from the measured variation in inlet pressure p_{in} as a function of time t as:

$$q = -V_{in}\frac{\mathrm{d}p_{in}}{\mathrm{d}t}. \tag{1}$$

The constant volume technique is used. Initially, the inlet chamber is filled with a gas at a pressure of about $p_{in} = 1$ atm; the valve is opened while the pump is working, with outlet pressure p_{out} kept significantly smaller than inlet pressure p_{in}, i.e. $p_{out} \ll p_{in}$. Then, pressure p_{in} is recorded 10 times per second for 10 hours. To calculate derivative $\mathrm{d}p_{in}/\mathrm{d}t$, function $\ln p_{in}(t)$ is interpolated by a fourth-order polynomial in seven time intervals separately. The interpolating coefficients ensure the continuity of the pressure and its derivative. Once the function

name of the structure	s_1	s_2	s_3	s_{static}	s_4	s_5	s_{10}	s_{12}	s_{0a}	s_{0b}
size d_2 [μm]	170	170	170	170	170	170	170	170	150	150
Intensity measurements	x	x	x	x						
measurements of p_{in} vs. time					x				x	
measurements of p_{out} vs. p_{in}						x	x	x		x
Figure number	8	8	8	8	4 (right), 12	5, 6, 7, 12	13	13	3, 4 (left)	5

Table 1: Structures and corresponding measurements.

dp_{in}/dt is obtained, the throughput is calculated using Eqs. (1). Throughput q can also be measured via outlet pressure p_{out} and pumping speed S using the relation

$$q = S\, p_{out}. \tag{2}$$

This method was used in [8], where the pumping speed was measured for an outlet pressure lower than 10^{-2}Pa using a mass spectrometer (QMG64 from Balzers). The following values were obtained: S =177, 206, 98, 88, and 65 L/s for H_2, He, N_2, Ar, and Xe, respectively. The two methods of determining throughput, the constant volume technique or via outlet pressure measurement, are compared in Sec.5.

2.3. Measuring ionization field intensity

In general, for the field ionization under partial pressure conditions, two different regimes are observed [4, 10]. In the low voltage regime, below 5 kV, the ionization is limited by the electric field. In the high-voltage regime, above 5 kV, the rate of ionization is limited by the gas supply, which also increases with voltage, resulting in an increase in current with voltage. In this regime, the probability of ionization of a molecule at a so-called "critical" distance (a few Armstrong) from the tip reaches 100%.

To measure ion current intensity, I, for an applied voltage, V, a pico-ammeter is directly connected to the tip and electrically grounded. Here, experiments are only performed at an extraction voltage of V = 12.0 kV. In this voltage regime, for the same voltage, the intensity depends only on the pressure. The measured I(V) characteristics, see also Ref.[8], confirm that a field ionization process occurs at the tip in the low-pressure chamber.

Four different experimental structures involving four different tips are shown here. All these structures use the same tube diameter d_2 = 170 μm but different tips and assemblies, which will be seen to induce roughly 50% uncertainty on the intensity value. For one of the four structures, measurements are performed at static pressure, which means that the gas is at rest near the tip. For the other three structures, measurements are carried out when the gas flows into the chamber through the coaxial structure.

3. Modeling gas flow

3.1. Definitions

In this section, the gas flow-field in the outlet chamber is obtained as a function of inlet pressure p_{in}. This requires knowing the gas flow rate $\dot{M}$, defined as the mass

of gas ΔM passing through a capillary during a time interval Δt.

$$\dot{M} = \frac{\Delta M}{\Delta t}. \tag{3}$$

Under this definition, no gas characteristics, like temperature and pressure, need to be specified, which is why it is widely used to report fundamental scientific results, see e.g. Refs.[16–18]. The throughput q is related to $\dot{M}$ as

$$q = \frac{1}{2} v_m^2 \dot{M}, \quad v_m = \sqrt{\frac{2R_g T}{\mathcal{M}}}, \tag{4}$$

where v_m is the most probable molecular speed at temperature T, R_g is the universal gas constant, $\mathcal{M}$ is the molar mass of a gas molecule. Since v_m depends on T, the value of q corresponds to some specific temperature T. The throughput q_0 through a thin orifice of area A in the free molecular flow regime is easily calculated as in [19]

$$q_0 = \frac{A v_m (p_{in} - p_{out})}{2\sqrt{\pi}}, \quad A = \pi(d_2^2 - d_1^2)/4. \tag{5}$$

This quantity depends on the gas species via the molar mass $\mathcal{M}$ and on the gas temperature T. Therefore, the dimensionless flow rate defined as

$$W = q/q_0 \tag{6}$$

is more appropriate to report theoretical and experimental results. This quantity actually becomes the transmission probability [20] in the free-molecular regime, which is gas-species-independent under diffuse gas-surface interaction. To determine the flow regime, the equivalent free path (EFP) of molecules ℓ is introduced via the gas viscosity μ, see e.g. [19]

$$\ell = \frac{\mu v_m}{p}. \tag{7}$$

Such a definition does not require knowledge of the molecular diameter, but is calculated directly via the macroscopic quantities. The viscosities of all gases considered here are given in Table 2. The gas rarefaction parameter δ, widely used in modeling rarefied gas flow, is defined as

$$\delta = h/\ell, \tag{8}$$

where h is a characteristic size of gas flow. For the flow in question, gap size $h = (d_2 - d_1)/2$ can be used in Eq.(8). Parameter δ is inversely proportional to the Knudsen number, so that the limit $\delta \to 0$ corresponds to the free-molecular regime, while the opposite limit $\delta \to \infty$ corresponds to the viscous regime.

3.2. *Flow-field around the tip: DSMC calculation*

The tip considered here is shown schematically in Figure 1. The direct simulation Monte Carlo (DSMC) method [19, 26] is applied to calculate the flow-field near the tip. The computational domain represents a cylinder with a length and radius of d_1. Since outlet pressure p_{out} is sufficiently low, the modeling can be performed assuming the free-molecular flow regime ($\delta = 0$). Experimental justifications for the free-molecular assumption are provided in Section 4.2. The distribution function of the generated particles is the Maxwellian, with a pressure p_0 and a temperature $T_0 = 300$ K at the exit of the coaxial structure. The pressure p_0 of the generated particles should provide the measured throughput q; thus, it is calculated via the dimensionless flow rate W as

$$p_0 = p_{in} W, \quad W = W(\delta_{in}), \tag{9}$$

Table 2: Properties of the gases under consideration: molecular weight $\mathcal{M}$, most probable speed v_m at $T_0 = 300$ K according to Eq.(4), dynamic viscosity μ at $T_0 = 300$ K taken from Refs.[21–25].

	H_2	He	Ne	N_2	Ar	Xe
$\mathcal{M}$(g/mol)	2.016	4.003	20.18	28.02	39.95	131.3
v_m (m/s)	1573	1116	497.2	421.9	353.4	194.9
μ (μPa s)	8.969	19.91	31.86	17.90	22.69	23.16

which depends on the rarefaction parameter δ_{in} calculated via p_{in} using Eqs.(7) and (8). Therefore, pressure p_0 is species-dependent. To model a more realistic distribution of particles entering the outlet chamber, the particles are generated inside the gap at a distance of $3h$ from the outlet. Diffuse scattering of particles on all solid surfaces is assumed. According to the scheme in Figure 1, the distance E between tip and extractor is about eight times larger than the tip size H. Moreover, the hole diameter ϕ is about six times larger than the tube diameter d_2, see Section 2. Given this distance and this diameter, these calculations do not need to take account of the extractor. Thus the free surfaces of the computational domain absorb all incident particles and do not emit particles into the domain. The number of samples was large enough to reduce the statistical scattering of the pressure to 0.1%.

3.3. *Flow-field around the tip: velocity distribution function*

Under some simplifying assumptions, the distributions of pressure, temperature, and bulk velocity along the symmetry axis can be obtained analytically. Disregarding the tip, i.e. in the configuration given in Figure 2, the annular outlet is assumed to emit particles that obey the Maxwellian distribution function corresponding to pressure p_0 and temperature $T_0 = 300$ K. Far from the outlet,

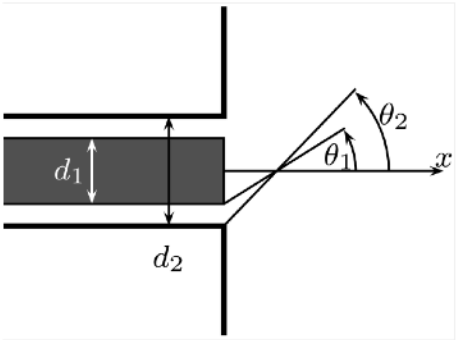

Figure 2: Scheme of the CIS outlet without tip used for analytical calculations.

the gas is assumed to be in equilibrium at pressure p_{out} and temperature T_0. Under such conditions, the distribution velocity function $f(x, \boldsymbol{v})$ at axis x is given as

$$f(x,\boldsymbol{v}) = \frac{e^{-(v/v_m)^2}}{\pi^{3/2}v_m^3}\begin{cases} n_0 & \text{at} \quad \boldsymbol{v} \in \Omega_0, \\ n_{out} & \text{at} \quad \boldsymbol{v} \in \Omega_{out}, \end{cases} \tag{10}$$

where $\boldsymbol{v}$ is the vector of gas molecular velocity, Ω_0 is the solid angle at which the annular outlet is visible, Ω_{out} is the remaining solid angle, n_0 and n_{out} are the number densities corresponding to pressures p_0 and p_{out}, respectively. Then, local number density n, bulk velocity u_x, and temperature T of the gas along the symmetry axis [19] are calculated via the distribution function (10) as

$$\begin{aligned}\frac{n(x)}{n_0} &= \frac{1}{n_0}\int f\,\mathrm{d}\boldsymbol{v} = \frac{n_{out}}{n_0} \\ &\quad + \frac{1}{2}\left(1 - \frac{n_{out}}{n_0}\right)(\cos\theta_1 - \cos\theta_2),\end{aligned} \tag{11}$$

$$\frac{u_x(x)}{v_m} = \frac{1}{n v_m} \int v_x f \, \mathrm{d}\boldsymbol{v} = \frac{n_0 - n_{out}}{2\sqrt{\pi}\, n(x)} \left(\sin^2 \theta_2 - \sin^2 \theta_1 \right), \tag{12}$$

$$\frac{T(x)}{T_0} = \frac{2}{3 n v_m^2} \int (\boldsymbol{v} - \boldsymbol{u})^2 f \, \mathrm{d}\boldsymbol{v} = 1 - \frac{2}{3} \left(\frac{u_x}{v_m} \right)^2. \tag{13}$$

Angles θ_1 and θ_2 shown in Figure 2 read

$$\tan \theta_1 = \frac{d_1}{2x}, \quad \tan \theta_2 = \frac{d_2}{2x}. \tag{14}$$

Local pressure is obtained from the state equation

$$\frac{p(x)}{p_0} = \frac{n(x) T(x)}{n_0 T_0}. \tag{15}$$

4. Results

4.1. Data on flow rate W measured via two techniques

Two measurement techniques are used here to obtain the dimensionless mass flow rate W (see Section 2). The first technique consists in a measurement of the inlet pressure. The experimental data regarding p_{in} as a function of time for helium, neon, argon, and xenon with structure s_{0a} ($d_2 = 150\,\mu$m) are shown in Figure 3 (a). For helium, the pressure drops by one order of magnitude during the first three hours, and then takes about ten hours more to lose another order of magnitude. The pressure variations for the other gases are even slower. The interpolating curves are represented by the black lines in Figure 3 (a). A relative difference between the experimental data and interpolations is plotted in Figure 3 (b), which gives an idea about the experimental error. The same measurements performed for hydrogen and nitrogen show similar behaviors, so the corresponding results are omitted in Figure 3.

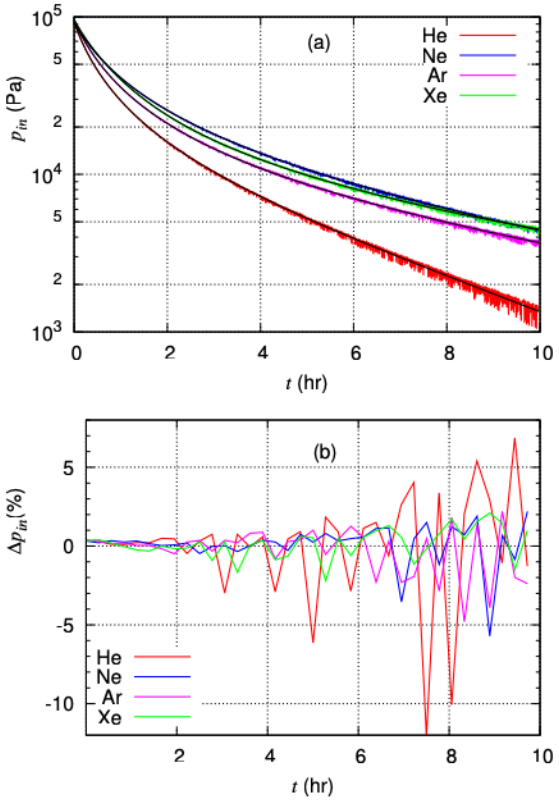

Figure 3: (a) Inlet pressure p_{in} vs. time t for $d_2 = 150\,\mu$m (s_{0a} in Table 1): colored lines - experiments, black lines - interpolation. (b) Relative difference $\Delta p_{in} = (p_{in}^{exp}/p_{in} - 1) \cdot 100\%$ between interpolation p_{in} and experimental p_{in}^{exp} data.

The interpolating parameters are described in Appendix A, the time intervals being selected to ensure continuity of pressure and of its derivative. The dimensionless flow rates W, calculated via Eqs. (1) and (6) using the interpolating formulas to obtain the time derivative from the values measured for $p_{in}(t)$, are plotted in Figure 4 (left) against the rarefaction parameter δ_{in}. This parameter was calculated from Eqs. (7) and (8) using the inlet pressure p_{in} and the data given in Table 2. Figure 4 (left) shows that W is almost identical for all gases considered here.

Therefore, once this quantity is measured for one gas it can be used for any other gas. When using the larger tube of diameter $d_2 = 170\ \mu$m, W was measured only for nitrogen, with results also shown in Figure 4 (right).

The experimental values for the flow rate W obtained by the second experimental procedure with structures s_{0b} and s_5, calculated using Eq. (2), are presented in Figure 5 versus the inlet rarefaction parameter δ_{in}. The behavior of W in the range $1 \le \delta_{in} \le 20$ is close to that plotted in Figure 4. A qualitative difference in its behavior is, however, observed for the largest values of δ_{in}, which will be shown to indicate a non-constant pumping speed over the outlet pressure range used in the experiment. Note that the results obtained for $d_2 = 150\ \mu$m and $170\ \mu$m are very similar. This perfectly illustrates the uncertainty due to manufacturing of the CIS and will be discussed in Section 5.1.

4.2. *Verification of free-molecular conditions*

Once the flow rate W is known, the assumption of free-molecular conditions in the outlet chamber can be verified. According to Eq. (9) and the results shown in Figure 4, pressure p_0 is about two orders smaller than p_{in}, while outlet pressure p_{out} is six orders smaller than p_{in}. This means that p_{out} can be neglected in the region near the tip but needs to be considered where it is far from the tip. The quantity p_0 obtained with the larger tube diameter $d_2 = 170\mu$m is plotted versus p_{in} in Figure 6 for all gases considered here (structure s_5). As can be seen, pressure p_0 is dependent on gas species. To verify the assumption on the free-molecular regime, the EFP ℓ_0 calculated via Eq. (7) for $p = p_0$ is plotted in Figure 7 versus the inlet pressure. The dashed horizontal line corresponds to gap size $h = 22.5\ \mu$m, so that the curves above this line correspond to the regime where $\ell_0 > h$ and intermolecular collisions can be ignored. It can be seen that collisions are negligible for almost the whole range of inlet pressure up to $p_{in} = 1.5 \times 10^4$ Pa for the light gases, namely, H_2, He, and Ne. For Xe, the regime is free-molecular up to $p_{in} = 4 \times 10^3$ Pa.

4.3. *Flow-field around the tip*

The flow-fields of local pressure p/p_0, temperature T (in Kelvin), and speed u/v_m calculated under the free-molecular conditions are shown in Figure 8. These quantities are the same for all gases under the condition $\ell_0 > h$. To obtain the pressure p for each gas species, the p_0 values given in Figure 6 should be used. As expected, pressure p sharply drops from p_0 at the outlet to $\approx 0.01 p_0$ at the tip, $x = 0.13$mm. Temperature also sharply drops from 300 K at the exit of the coaxial structure to about 80 K at the tip. The temperature is even lower (less than 50 K) in the region far from both outlet and tip. This behavior is typical of an expanding gas. The dimensionless gas speed u/v_m has the magnitude order of the Mach number. According to Figure 8, the flow becomes transonic far from the structure's exit in the outlet chamber.

The functions $p(x)/p_0$, $u_x(x)/v_m$, and $T(x)$ given by Eqs. (11) - (15) are plotted in Figure 9 for two typical values of $p_{out}/p_0 = 10^{-4}$ and 10^{-5} in the range $0.1 \le x(\text{mm}) \le 1$. The left and right limits correspond to the tip and extractor positions, respectively. It can be seen

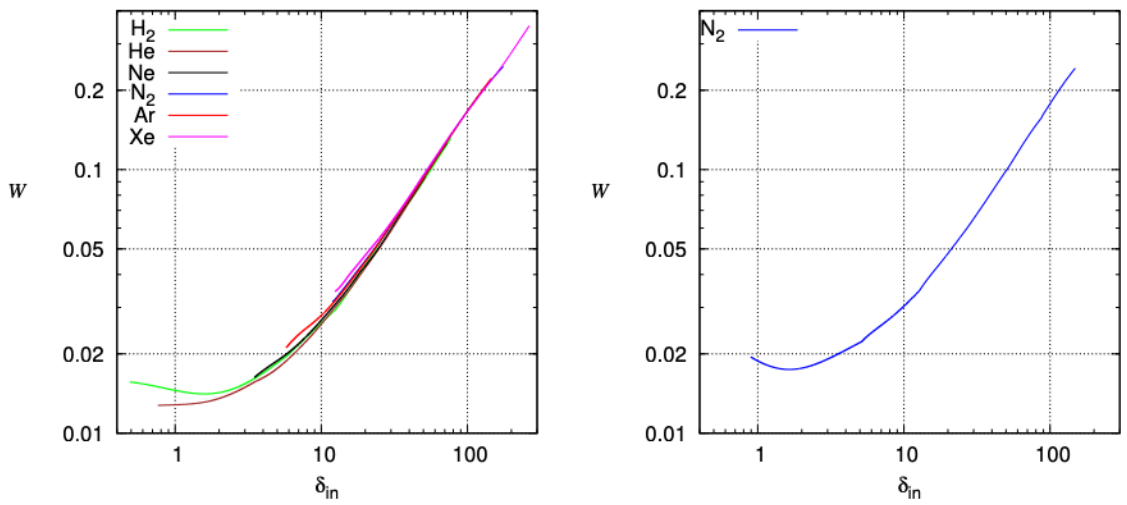

Figure 4: Dimensionless flow rate W calculated via measured and then interpolated function $p_{in} = p_{in}(t)$ vs. rarefaction parameter δ_{in}: left - structure s_{0a}, $d_2 = 150\ \mu$m, right - structure s_4, $d_2 = 170\ \mu$m.

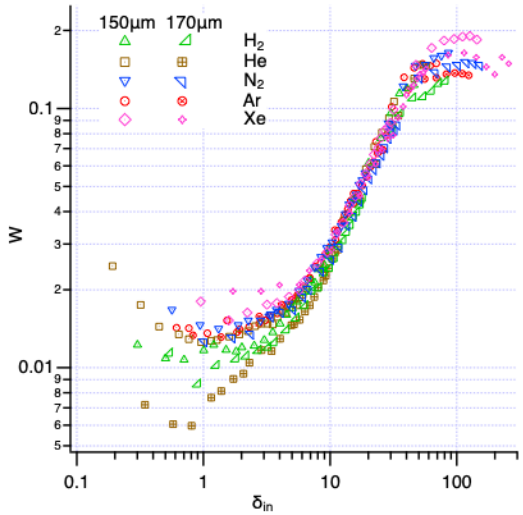

Figure 5: Dimensionless flow rate W obtained from measured pumping speed S and outlet pressure p_{out}, calculated via Eq.(2) vs. rarefaction parameter δ_{in} for structures s_{0b} ($d_2 = 150\ \mu$m) and s_5 ($d_2 = 170\ \mu$m).

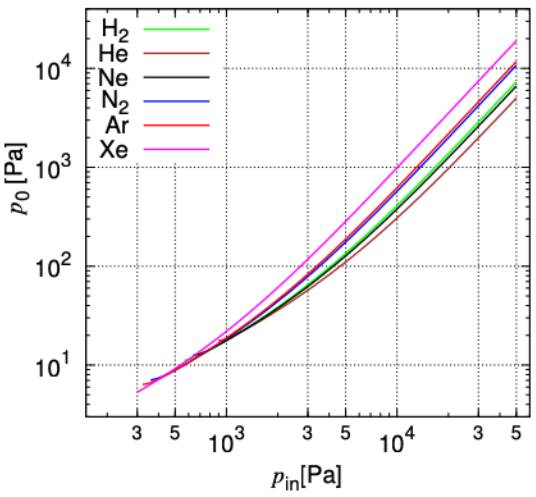

Figure 6: Pressure p_0 vs. inlet pressure p_{in} for $d_2 = 170\ \mu$m.

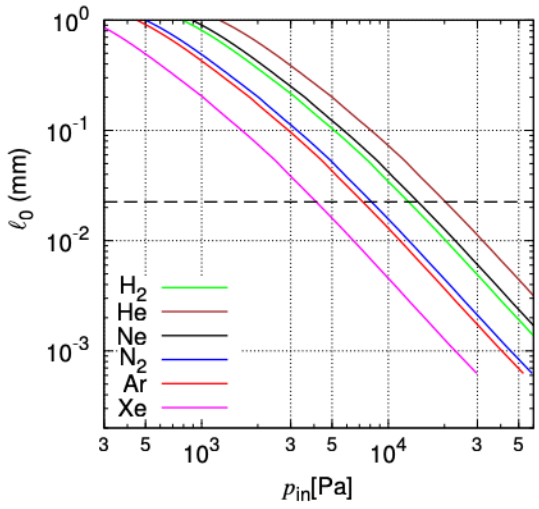

Figure 7: Equivalent free path ℓ_0 vs. inlet pressure p_{in} for $d_2 = 170\ \mu$m. The dashed horizontal line represents gap size.

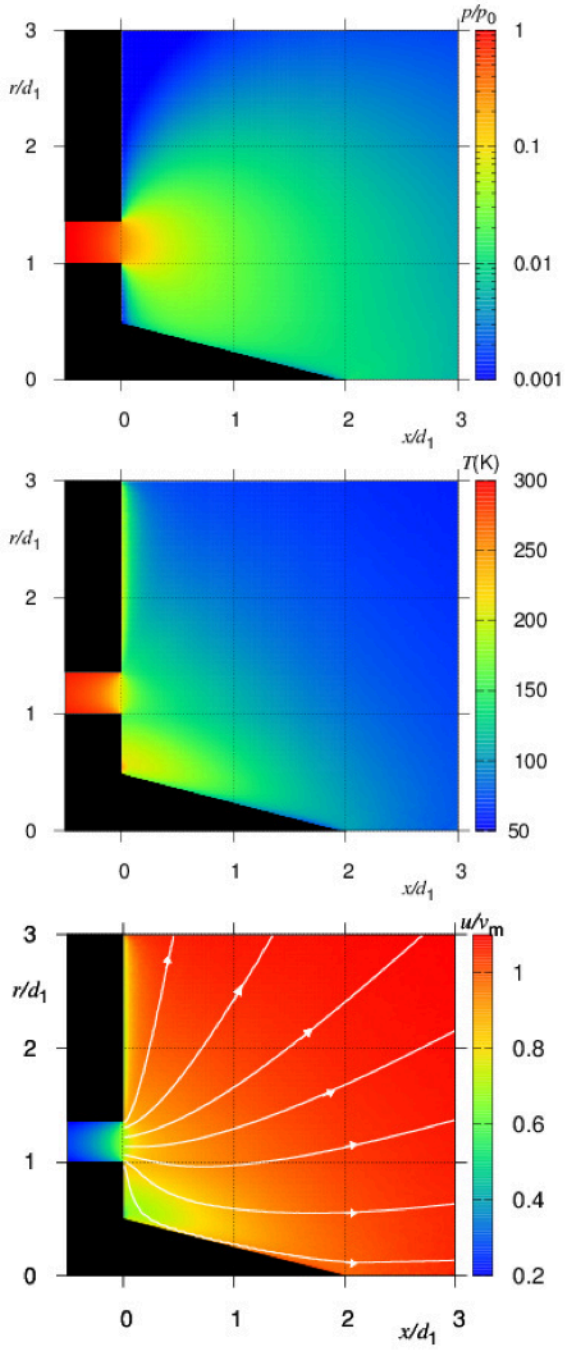

Figure 8: Flow-field in the outlet of tube of diameter $d_2 = 170\ \mu$m: top - pressure p/p_0, middle - temperature in K, bottom - local speed u/v_m where v_m corresponds to $T_0 = 300$ K.

that pressure $p(x)$ sharply decreases just near the tip, then smoothly tends toward p_{out} far from the coaxial structure's exit in the outlet chamber. The velocity $u_x(x)$ near the tip is close to v_m and then slightly increases up to $1.1v_m$. The temperature near the tip is almost half that of $T_0 = 300$ K and then continues to drop until it reaches about 50 K. The influence of the value of p_{out}/p_0 on all these functions becomes significant starting from the position $x = 0.5$ mm and it increases farther from the tip. The asymptotic behavior of $p(x)$, $u_x(x)$, and $T(x)$ far from the tip can be obtained from Eqs. (11) - (15) at $x >> d_1$. Under this condition, both θ_1 and θ_2 become small, so that $n(x) \to n_{out}$, $u_x(x) \to 0$, $T(x) \to T_0$, and $p(x) \to p_{out}$. For the purposes of comparing the analytical solution (11) - (15) with the Monte Carlo results, the latter are shown in Figure 9 by symbols. The comparison shows that the two solutions

almost coincide. Thus, the analytical solution obtained in the absence of the tip describes well the flow-field past the tip along the symmetry axis.

4.4. *Ion current intensity*

Figure 10 shows how the intensity of the ion current emitted by field ionization depends on the pressure measured in the low-pressure chamber, p_{out}, for four different experimental structures, see Section 2.3. One experiment, denoted s_{static} (brown triangles), is performed at static pressure. The other three, denoted s_1, s_2, and s_3 (blue, green, and orange symbols), are carried out when the gas flows into the chamber through the coaxial structure. It is worth to note that there is one outlier point when the intensity is measured with s_3 configuration. This fact can be explained by the evolution of the tip shape during the pressure measurement, because the palladium layer covered the tip is not stable. This hypothesis was confirmed by the measurements of I(V) characteristics and by the SEM observation of the tip after the experiment.

The straight line in Figure 10 corresponding to the intensity without the gas flow indicates a linear dependence of the current on the pressure near the tip, which is equal to the outlet pressure p_{out} in this case. Since p_{out} is known, these data are used as an intensity calibration. The straight lines corresponding to s_1, s_2 and s_3 are shifted to the left with respect to the data for s_{static} by a factor of 300, i.e. the pressure p_{tip} is always proportional to p_{out}. The intensity variation obtained for different structures is approximately 50% so that the pressure near the tip p_{tip} is related

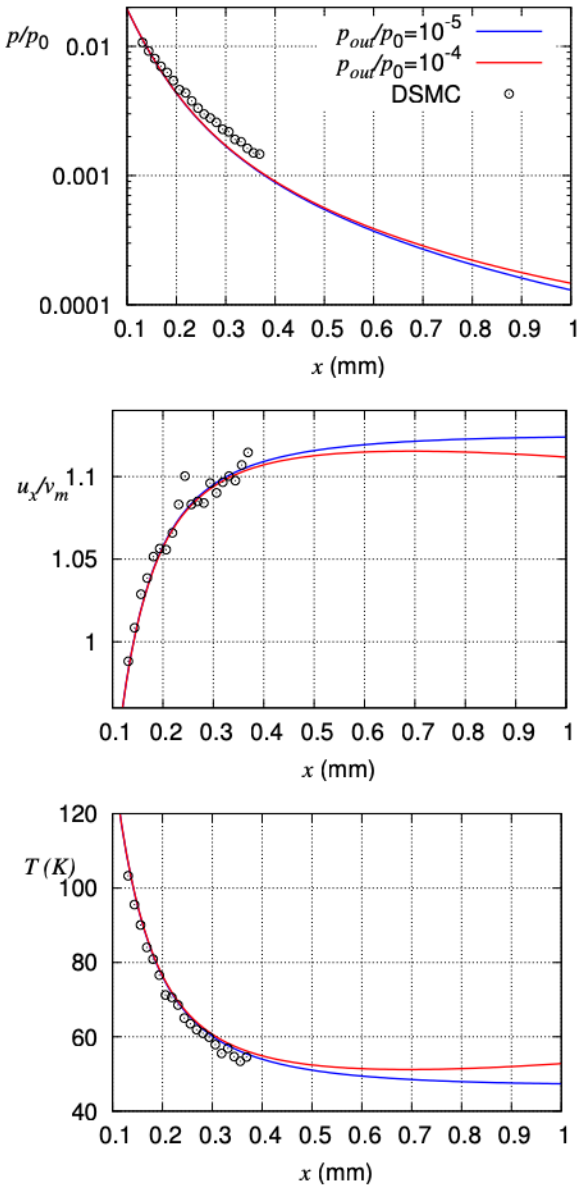

Figure 9: Local pressure p/p_0, bulk velocity u_x/v_m, and temperature T vs. coordinate x for $d_2 = 170$ μm. The values of p_0 are plotted in Figure 6 against p_{in}. The value of v_m is given in Table 2.

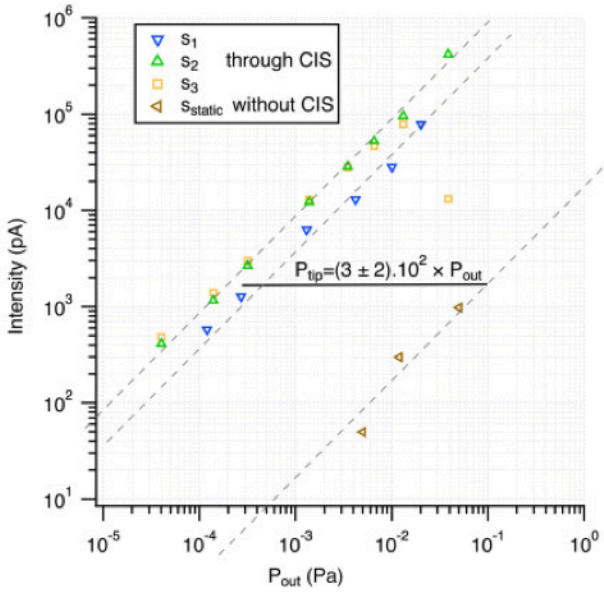

Figure 10: Intensity measurements for 4 different structures, s_1, s_2, s_3 and s_{static}, with tube diameter $d_2 = 170\ \mu$m: notations s_1, s_2, and s_3 correspond to the cases when a gas flows through CIS; notation s_{static} corresponds to the case of gas at rest. The black line shows the shift of pressure indicating the ratio between the local pressure at the tip p_{tip} and the outlet pressure p_{out}.

to p_{out} as

$$p_{tip} = (3 \pm 2) \times 10^2 p_{out}. \tag{16}$$

5. Discussion

5.1. Uncertainty on local pressure deduced from flow rate

In this section, the empirical formula (16) is compared with the modeled gas pressure at the tip obtained from Eq. (15). The measured input data used to calculate this local pressure involve uncertainties which affect the pressure value obtained. The following measured data are used to calculate the pressure near the tip. Inlet pressure p_{in} and volume of inlet tank V_{in} are used to calculate throughput q. Dimensionless flow rate W is obtained via the cross-sectional area, A, see Eq.(5), using tube and wire diameters d_1 and d_2, respectively and, for some measurements, outlet pressure p_{out}. Two other factors, pumping speed and difference in structure assemblies, impact the local pressure values. Below, all sources of uncertainty are analyzed, and its budget is presented.

Throughput was calculated from Eq. (1) using the variation in inlet pressure with time and the volume V_{in}. The 17% volume uncertainty directly affects the uncertainty on tip pressure p_{tip}.

The dimensionless flow rate W is defined by Eq. (6) via free-molecular throughput q_0, which is proportional to area A, see Eq.(5). Its relative uncertainty, u_A, is related to those of tube and wire diameters u_{d_1} and u_{d_2}, respectively, as

$$u_A = 2\frac{\sqrt{d_2^4 u_{d2}^2 + d_1^4 u_{d1}^2}}{d_2^2 - d_1^2} = 0.42 \tag{17}$$

where $u_{d1} = 0.1$ and $u_{d2} = 0.08$.

As shown in Table 1, the inlet pressure measurements involved in calculations both of throughput and of q_0 are performed using a different structure from that used for the intensity measurements. Figure 5 indicates that with a different diameter d_2, the function of flow rate W vs. the gas rarefaction parameter is similar. However, this flow rate W should depend on the characteristic size of gas flow through the rarefaction parameter, which is a function of h. Considering the positive uncertainties on d_2, the uncertainty on h gives $h_1 = (20 \pm 10)\ \mu$m and $h_2 = (30 \pm 10)\ \mu$m. The value of h strongly impacts the gas rarefaction parameter δ_{in} and the value of W is also weakly sensitive to h,

which explains the apparently similar curves even for two different structures. We therefore needed to estimate the variation in flow rate due to the structure. To this end, we chose to vary the dimensionless flow rate W obtained with different structures assembled with $d_2 = 170\mu$m, using throughput characterizations for four different structures (s_4, s_5, s_{10}, and s_{12}), three of them determined via outlet pressure measurement. In such cases, the pumping speed used to calculate W with Eq. (2) should be corrected. The difference in dimensionless flow rate observed for higher pressures and presented in Figures 4 and 5 is due to the non-constant pumping speed over the considered outlet pressure range. Indeed, if we calculate pumping speed from the throughput q calculated using inlet pressure variation and plotted in Figure 4, then pumping speed S is not constant. Quantity S is plotted against EFP ℓ_{out} based on outlet pressure p_{out} in Figure 11. It can be seen that pumping speed S is close to the measured values, the dashed lines in Figure 11, provided EFP is large enough (see also Section 2.2 for the measured values of S). However, the recalculated values of S decrease with decreasing EFP and then increase when $\ell_{out} < 0.4$ m. This behavior of pumping speed was predicted in Ref. [27].

Once pumping speed S is known as a function of output pressure using the data plotted in Figure 11 and data for p_{in} vs. p_{out} for $d_2 = 170\ \mu$m, throughput q is calculated from Eq. (2). Then flow rate W is calculated from Eq. (6) and plotted against δ_{in} in Figure 12. In the range $\delta_{in} < 30$, the flow rate W agrees with that plotted in Figure 5 (right). However, the flow rate W plotted in Figure 4 (right) is slightly larger than that plotted in Figure 12.

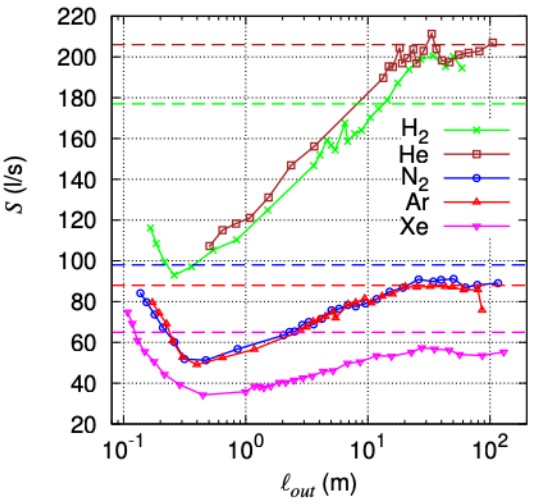

Figure 11: Pumping speed S calculated via throughput q for a tube diameter of 150 μm vs. outlet EFP ℓ_{out}. The dashed lines are the measured pumping speed for each gas.

This is because the structures have the same dimensions, but they are from different assemblies. The pressure measurement error also contributes in the difference of W, but not significantly. We have seen that the value of W is weakly sensitive to tube diameter d_2.

To estimate the influence of the configuration on flow rate W, experimental data p_{out} vs. p_{in} for different configurations can be used. Since the procedure used to calculate W from p_{out}/p_{in} is the same for all configurations, the relative difference in p_{out} for a fixed p_{in} is equal to the relative variation in W for a fixed δ_{in}. The relative deviations of the W of two different structures from a third structure are plotted in Figure 13. The maximum variation is 25%, which can be considered to represent the uncertainty due to both sources: uncertainty of structure and uncertainty of pressure measurement. As is shown in Figure 3, the

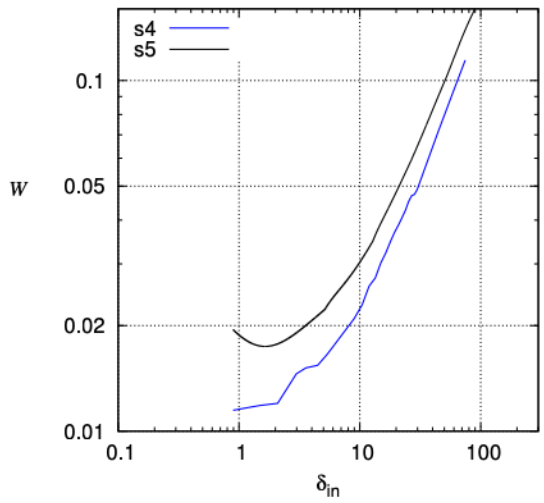

Figure 12: Dimensionless flow rate W for $d_2 = 170\ \mu$m calculated via S given in Figure 11 vs. parameter δ_{in}. Black line corresponds to that given in Figure 4.

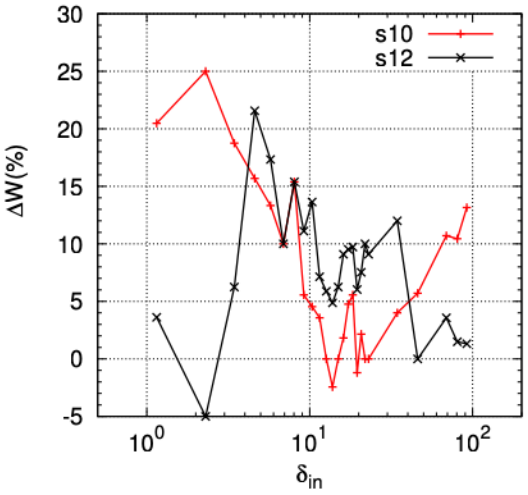

Figure 13: Relative variation in W for different configurations at $d_2 = 170\ \mu$m.

inlet pressure oscillation does not exceed 11%. The oscillation of the outlet pressure is even smaller so that the uncertainty shown in Figure 13 is mostly due to the structure.

In the experiment, the position of the tip (see Figure 1) is set at $H = (130 \pm 10)\ \mu$m, i.e., its uncertainty is 7.7%. This leads to an uncertainty of 15% on local pressure, $u_H = 0.15$, taking into account the pressure variation along the symmetry axis shown in Figure 9.

The combined uncertainty u is calculated, based on all the above uncertainties, as

$$u = \sqrt{u_s^2 + u_V^2 + u_H^2 + u_A^2} = 0.54 \qquad (18)$$

The budgets of uncertainties and combined uncertainty are summarized in Table 3.

Table 3: Budget of relative uncertainties.

source	reference	value
structure	Fig.13	u_s =0.25
volume V_{in}	–	$u_V = 0.17$
tip position H	Fig.9	$u_H = 0.15$
area A	Eq.(17)	$u_A = 0.42$
combined uncertainty	Eq.(18)	$u = 0.54$

5.2. *Field ionization intensity vs. gas flow modeling*

Pressure at the tip is plotted versus outlet pressure in Figure 14. The theoretical values were calculated from Eq.(15) at the tip position ($x = H$), where p_0 is given by Eq. (9) and W is obtained from inlet and outlet pressure measurements. The experimental values of p_{tip} were extracted from the data presented in Figure 10. The theoretical and experimental results are in good agreement considering the number of orders of magnitude between the inlet and outlet pressures (6 to 7 orders of magnitude). Figure 14 shows that the ionization intensity indicates a

pressure at the tip of about $(3 \pm 2) \times 10^2$ times the outlet pressure, while the gas flow modeling gives a pressure at the tip of about $(8 \pm 3) \times 10^2$ times the outlet pressure, thus higher than that measured. However, given the uncertainties described above, the theoretical and experimental values are very similar. Therefore, gas flow does not cause a significant drop in ionization intensity. This does not mean that there is no recombination at the tip, but that reading the relative intensity gives an indication of the local pressure. To draw any real conclusions about the physical mechanisms occurring at the tip, it seems essential to measure the spread of the ion beam energy.

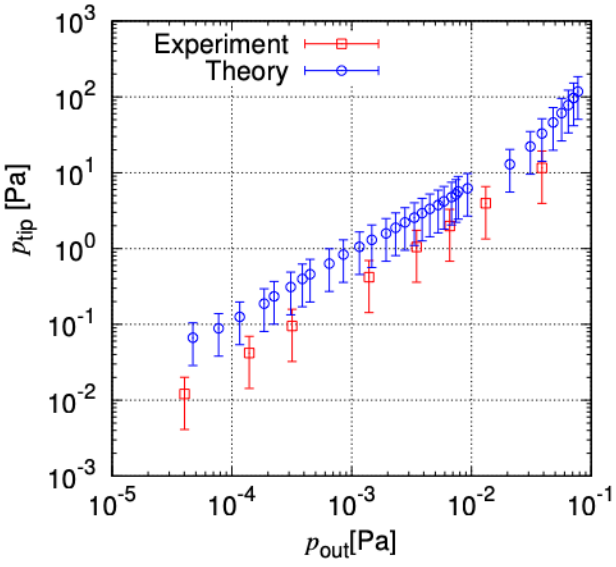

Figure 14: Local pressure p_{tip} at the tip position vs. outlet pressure p_{out}.

5.3. Precision of the tip as local gauge

The results presented above suggest that a field ion tip can reliably be used as a local pressure gauge. With a fixed tip position, as in these experiments, local pressure is measured with reasonable precision in a volume of about $10 \times 10 \times 10$ μm^3 around the tip.This value is estimated from relatively precise tip positioning under the optical microscope. For greater precision, these experiments should be performed with the same tip made from a noble metal to ensure high repeatability between intensity measurements, and using a piezo actuator to place, and if necessary move, the tip in the gas expansion. The emission zone of a metal tip corresponds to the last part of the tip: a half-sphere 100 nm in diameter. This is the place where ionization takes place, and where the electric field is sufficiently intense to produce field ionization. To perform higher-resolution measurements, we propose the following steps: register ion beam intensity with a tip for some known pressure and then use the same tip in a plume of a gas, moving it to perform pressure mapping. We assume that this procedure is possible if radiative recombination is not dominant, i.e. when the EFP is sufficiently small, $\ell < 10$ μm.

6. Conclusion

After re-exploring the gas flow rate through the coaxial ion source by the constant volume method, we studied the expansion of the gas into the outlet chamber both via the DSMC method and via an analytical method using the velocity distribution function. This allowed us to obtain the distribution of pressure near the tip, especially in the emission zone of the field ionization tip. The DSMC and analytical methods yield reasonably similar results in the zone considered in this paper, i.e. for a distance up to

100 μm from the exit of the tube. From these results and considering the dispersion in the structure assembly due to manufacturing precision regarding tubes and wires, the pressure in the emission zone is estimated to be $(8 \pm 3) \times 10^2$ times the pressure in the outlet chamber.

The intensity ratio measured with the tip, with or without using the coaxial structure to inject the gas into the outlet chamber, indicates that when using it the pressure in the emission zone is $3 \pm 2 \times 10^2$ times the pressure in the outlet chamber. Thus, both calculated pressure and that measured through the intensity of field ionization are of the same order of magnitude. In the light of these results, we can conclude that the pressure at the tip is reliably measured through field ion intensity using a metal tip, even in an expanding gas. It has been shown that the pressure is measured with high spatial resolution: a tiny cube having an edge of 10 μm. This size depends on the precision of the optical microscope in positioning the end of the tip where measurement takes place. Considering the size of the emission zone on the tip (a sphere 100 nm in diameter), this procedure could constitute a very precise local pressure gauge if radiative recombination does not become dominant. Summarizing, we have shown that a field ionization tip can be considered as a local pressure gauge with a current spatial resolution of 10 μm that can be further improved. Based on this work and experimental verification, several extensions appear of interest. First, gas-flow modeling will help to optimize the position of the tip at the exit of the coaxial structure so as to achieve the highest intensity beam without radiative recombination. Second, in a different field, our work suggests that a field ionization tip can be useful to measure local pressure in gas jets.

CRediT authorship contribution statement

Felix Sharipov: Software, Formal analysis, Visualization, Writing – original draft, Writing – review & editing.

Irina Graur: Formal analysis, Visualization, Writing – review & editing

Evelyne Salançon: Conceptualization, Methodology, Investigation, Data curation, Visualization, Writing - Original Draft, – review & editing

Declaration of competing interest

The authors declare that they have no known competing financial interests or personal relationships that could have appeared to influence the work reported in this paper.

Acknowledgments

F.S. thanks CNPq, Brazil for supporting his research (grant No 303429/2022-4). The authors would like to thank Djouher Bedrane for some of the field ionization intensity measurements used and Marjorie Sweetko for improving the English of this article.

References

[1] M. Petrenko, S. Bobashev, G. Tumakaev, A method for determination of spatial distribution of gas concentration in supersonic jets outflowing into vacuum, Tech. Phys. Lett. 43 (2017) 428–430. doi:10.1134/S1063785017050091.

[2] J. Yu, V. Vuorinen, O. Kaario, T. Sarjovaara, M. Larmi, Visualization and analysis of the characteristics of transitional underexpanded jets, International Journal of Heat and Fluid Flow 44 (2013) 140–154. doi:10.1016/j.ijheatfluidflow.2013.05.015.

[3] A. Y. Chang, B. E. Battles, R. K. Hanson, Simultaneous measurements of velocity,temperature, and pressure using rapid cw wavelength-modulation laser-induced fluorescence of oh, OPTICS LETTERS 15 (12) (1990) 706. doi:10.1364/OL.15.000706SMASH.

[4] E. W. Müller, T. T. Tsong, Field Ion Microscopy: Principles and Applications, American Elsevier Pub. Co, 1969. doi:10.1016/S0079-6816(74)80005-5.

[5] R. Gomer, Field Emission and Field Ionization, American Institute of Physics, 1992.

[6] J. J. Hren, S. Ranganathan (Eds.), Field-Ion Microscopy, Springer, 1968. doi:10.1007/978-1-4899-6513-4.

[7] J. Orloff, L. W. Swanson, An asymmetric electrostatic lens for field-emission microprobe applications, J. Appl. Phys. 50 (4) (1979) 2494–2501. doi:10.1063/1.326260.

[8] D. Bedrane, A. Houël, A. Delobbe, M. Lagaize, P. Dumas, S. Veesler, E. Salan¸c on, Coaxial ion source: Pressure dependence of gas flow and field ion emission, J. Vac. Sci. Technology B 41 (4) (2023) 042808. doi:10.1116/6.0002795.

[9] M. Konishi, M. Takizawa, T. Tsumori, Characteristics of a helium field ion gun, J. Vac. Sci. Technol. B 6 (1) (1988) 498–501. doi:10.1116/1.584051.

[10] K. Jousten, K. Bohringer, S. Kalbitzer, Current-voltage characteristics of a gas field ion source, Appl. Phys. B 46 (1988) 313–323.

[11] E. Salançon, Z. Hammadi, R. Morin, A new approach to gas field ion sources, Ultramicroscopy 95 (2003) 183–188. doi:10.1016/S0304-3991(02)00315-7.

[12] M. Descoins, Z. Hammadi, R. Morin, Local supply of gas in vacuum: Application to a field ion source, Journal of Vacuum Science & Technology A 26 (2008) 1331. doi:10.1116/1.2968689.

[13] Z. Hammadi, M. Descoins, E. Salançon, R. Morin, Proton and light ion nanobeams from field ionization of water, Applied Physics Letters 101 (2012) 243110. doi:10.1063/1.4770516.

[14] L. Lapena, D. Bedrane, A. Degiovanni, E. Salançon, Bright sources under the projection microscope: using an insulating crystal on a conductor as electron source, The European Physical Journal: Applied Physics 97 (13) (2022). doi:10.1051/epjap/2022210260.

[15] K. Jousten (Ed.), Handbook of Vacuum Technology, 2nd Edition, WILEY-VCH, Weinheim, 2016.

[16] I. Graur, F. Sharipov, Gas flow through an elliptical tube over the whole range of the gas rarefaction, Eur. J. Mech. B / Fluids 27 (3) (2007) 335–345. doi:10.1016/j.euromechflu.2007.07.003.

[17] I. Graur, A. P. Polikarpov, F. Sharipov, Numerical modelling of rarefied gas flow through a slit at arbitrary gas pressure ratio based on the kinetic equation, Z. Angew. Math. Phys. (ZAMP) 63 (2012) 503–520. doi:10.1007/s00033-011-0178-4.

[18] F. Sharipov, *Ab initio* simulation of gaseous mixture flow through an orifice, Vacuum 143 (2017) 106–118. doi:10.1016/j.vacuum.2017.05.030.

[19] F. Sharipov, Rarefied Gas Dynamics. Fundamentals for Research and Practice, Wiley-VCH, Berlin, 2016. doi:10.1002/9783527685523.

[20] F. Sharipov, V. Seleznev, Data on internal rarefied gas flows, J. Phys. Chem. Ref. Data 27 (3) (1998) 657–706. doi:10.1063/1.556019.

[21] M. J. Assael, S. Mixafendi, W. A. Wakeham, The viscosity and thermal conductivity of normal hydrogen in the limit of zero density, J. Phys. Chem. Ref. Data 15 (4) (1986) 1315–1322. doi:10.1063/1.555764.

[22] W. Cencek, M. Przybytek, J. Komasa, J. B. Mehl, B. Jeziorski, K. Szalewicz, Effects of adiabatic, relativistic, and quantum electrodynamics interactions on the pair potencial and thermophysical properties of helium, J. Chem. Phys. 136 (22) (2012) 224303. doi:10.1063/1.4712218.

[23] W. A. Cole, W. A. Wakeham, The viscosity of nitrogen, oxygen, and their binary-mixtures in the limit of zero density, J. Phys. Chem. Ref. Data 14 (1) (1985) 209–226. doi:10.1063/1.555748.

[24] F. Sharipov, V. J. Benites, Transport coefficients of argon and its mixtures with helium and neon at low density based *ab initio* potentials, Fluid Phase Equilibria 498 (2019) 23–32. doi:10.1016/j.fluid.2019.06.010.

[25] F. Sharipov, V. J. Benites, Transport coefficients of isotopic mixtures of noble gases based on *ab initio* potentials., Phys. Chem. Chem. Phys. 23 (2021) 16664–16674. doi:10.1039/D1CP01971F.

[26] G. A. Bird, Molecular Gas Dynamics and the Direct Simulation of Gas Flows, Oxford University Press, Oxford, 1994. doi:10.1093/oso/9780198561958.001.0001.

[27] F. Sharipov, Numerical simulation of turbomolecular pump over a wide range of gas rarefaction, J. Vac. Sci. Technol. A 28 (6) (2010) 1312–1315. doi:10.1116/1.3484139.

Appendix A. Interpolation

The whole period of the experiment t_{exp} was divided into seven intervals

$$t_{i-1} \le t \le t_i, \quad 1 \le i \le 7, \tag{A.1}$$

where $t_0 = 0$ and $t_7 = t_{exp}$. In each interval, the pressure is interpolated by the function

$$p_{in}(t) = p_{in}(0) \exp\left[-\sum_{j=0}^{4} a_{ij}(t - t_{i-1})^j\right], \tag{A.2}$$

where $a_{10} = 0$. Coefficients a_{1j} $(1 \le j \le 4)$ are obtained by the least square method in the interval $0 \le t \le t_1$. Then, coefficients a_{i0} and a_{i1} $(2 \le i \le 7)$ are obtained from the continuity condition of the pressure and its derivative

$$a_{i0} = \sum_{j=0}^{4} a_{i-1,j}(t_{i-1} - t_{i-2})^j, \tag{A.3}$$

$$a_{i1} = \sum_{j=1}^{4} j a_{i-1,j}(t_{i-1} - t_{i-2})^{j-1}, \tag{A.4}$$

while the remaining coefficients a_{ij} $(2 \le j \le 4)$ are obtained by the least square method in the intervals $t_{i-1} \le t \le t_i$ $(2 \le i \le 7)$. Then, the throughput q and dimensionless flow rate W are given as

$$q(t) = V_{in} p_{in}(t) \sum_{j=1}^{4} j a_{ij}(t - t_{i-1})^{j-1}, \tag{A.5}$$

$$W(t) = \frac{8V_{in}}{\sqrt{\pi}(d_2^2 - d_1^2)v_m} \sum_{j=1}^{4} j a_{ij}(t - t_{i-1})^{j-1}. \tag{A.6}$$

Using Eqs.(A.2) and (A.6), the function $W = W(\delta_{in})$ is plotted.